Visual Informatics 3 (2019) 69–80

Contents lists available at ScienceDirect

Visual Informatics

journal homepage: www.elsevier.com/locate/visinf

Direct design to stress mapping for cellular structures

Liangchao Zhu, Ming Li *, Weiwei Xu

State Key Laboratory of CAD&CG, Zhejiang University, Hangzhou, 310058, China

ARTICLE INFO

Article history:
Received 27 June 2019
Accepted 1 July 2019
Available online 19 July 2019

Keywords:
Instant simulation
Parametric solution
Cellular structures
Proper generalized decomposition (PGD)
Model reduction

ABSTRACT

This paper aims to *instantly* predict within *any* accuracy the stress distribution of cellular structures under parametric design, including the shapes or distributions of the cell geometries, or the magnitudes of external loadings. A classical model reduction technique has to balance the simulation accuracy and interaction speed, and has difficulty achieving this goal. We achieve this by computing offline a *design-to-stress mapping* that ultimately expresses the stress distribution as an explicit function in terms of its design parameters. The mapping is determined as a solution to an extended finite element analysis problem in a high-dimension space, including both the spatial coordinates and the design parameters. The well-known curse of dimensionality intrinsic to the high-dimension problem is (partly) resolved through a spatial separation using two main techniques. First, the target mapping takes a reduced form as a sum of the products of separated one-variable functions, extending the proper generalized decomposition technique. Second, the simulation problem in a varied computation domain is reformulated as that in a fixed-domain, taking an integration function as the sum of the products of separated one-variable functions, in combination with high-order singular value decomposition. Extensive 2D and 3D examples are shown to demonstrate the approach's performance.

1. Introduction

Mimicking the nature and design of cellular structures possessing certain geometric and physical properties has long been a pursuit, and has significant potential applications in the medical, materials, and aerospace fields, as well as in national defense (Ashby and Medalist, 1983; Gibson and Ashby, 1997; Fleck et al., 2010; Regli et al., 2016). The recent and fast developments of additive manufacturing technologies have also overcome the difficulty of accurately advocating such complex structures and further boosted their intensive studies and wide industrial applications. For example, the leading 3D printing server Materialise Magics provides 28 types of cellular cells for a structural interior design, parts of which are shown in Fig. 2.

Despite such industrial potential and technical developments, the design of a digital cellular structure satisfying industrial requirements remains an extremely challenging task. Traditional design approaches mainly rely on tedious repeated modifications, namely, the designers repeatedly regenerate the designs, simulate their properties, and determine the next design options. In contrast, optimization-based design approaches (Rodrigues et al., 2002; Sigmund and Maute, 2013; Panetta et al., 2015; Schumacher et al., 2015; Wu et al., 2018; Zhu et al., 2017) are able to significantly reduce the amount of required human interactions, although they also limit the designer's freedom of choice. Designers typically incorporate their intuition and expertise as part of the design process, and can instantly predict the properties of a structure once the modifications are applied, freely exploring the candidate choices for deeper insight and accelerated production. The trend of such an *interactive simulation* has also been recognized and adopted by leading CAD/CAE providers, for example, Discovery Live recently released by ANSYS, or DreamCatcher by AutoCAD. However, these software titles only work on solid structures at the macro-scale and are mainly based on powerful computational facilities. An interactive simulation of cellular structures involves hugely complex structures of much higher degrees of freedom, and to the best of our knowledge, no previous approaches have been proposed on this topic.

We hope to resolve this issue under two key requirements: an instant simulation for any type of complex cellular structures under modification, and under any simulation accuracy control. It is assumed here that the candidate design parameters have been prescribed in advance by the designers, including the shapes or overall distributions of the microstructures and the magnitudes of the external loadings. Classical techniques on a model reduction or brute force fitting have difficulty achieving this goal; the former has to balance the simulation accuracy and interaction speed, whereas the latter generating such a fitting function in a high-dimensional space is non-trivial, as will be further explained in Section 2. The challenging goal is achieved here by building

* Corresponding author.
E-mail address: liming@cad.zju.edu.cn (M. Li).
Peer review under responsibility of Zhejiang University and Zhejiang University Press.

https://doi.org/10.1016/j.visinf.2019.07.002

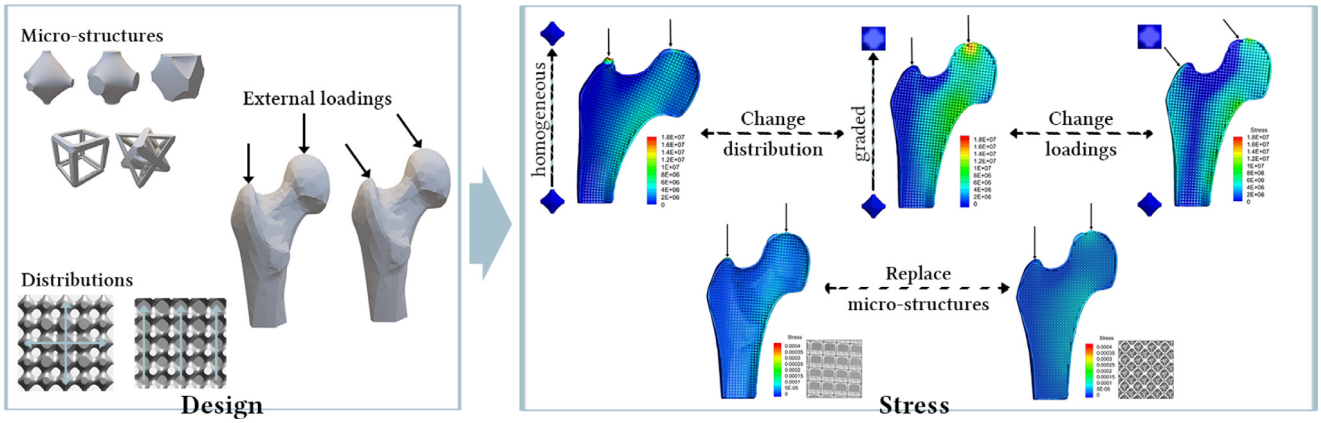

Fig. 1. A direct design-to-stress mapping for cellular structures was built. The design choices include changing the shapes or distributions of the microstructures, or the magnitude of the external loadings. Once the mapping is obtained offline, an online simulation of the cellular structures can be achieved instantly through a simple functional evaluation. The mapping is established as a computing solution to the high-dimensional finite element (FE) analysis problem proposed herein.

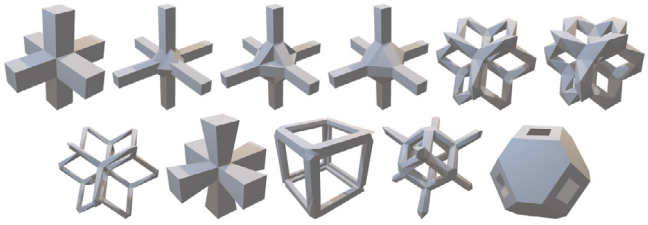

Fig. 2. Orthotropic microstructures from Materialise Magics.

offline a mapping directly from all of the design parameters to the structural stress distributions under any simulation accuracy control. Once the mapping is obtained, the stress distribution at a specific design prescription is acquired through a simple functional evaluation and can be achieved instantly.

The target design-to-stress mapping for cellular structures is established by conducting a bi-scale FE analysis in a high-dimensional space containing both the spatial coordinates and the design parameters. Solving this problem incurs the intrinsic difficulty of the well-known curse of dimensionality (Ammar et al., 2006), namely, the number of degrees of freedom will expand exponentially with respect to the number of dimensions. We further resolve this issue based on a spatial separation strategy. Specifically, domain of varying shape is transformed into a fixed domain representing the target solution and all involved integration functions as the sum of products of one-variable functions by extending the novel model reduction approach, namely, proper generalized decomposition (PGD) (Ammar et al., 2006, 2007; Chinesta et al., 2010, 2011b), and a high-order singular value decomposition technique (HOSVD). Once the spatial separation is achieved, the curse of dimensionality is resolved, and the direct design-to-stress mapping can then be similarly derived as a classical FE analysis without much difficulty, as explained in the following sections. The PGD approach was further extended to structures of varied topology in our previous study (Zhu et al., 2016) using R-function (Shapiro, 1991; Rvachev and Sheiko, 1995). Related to the study, Lamari et al. (2010) also used PGD for efficient homogenization, treating the material properties as design variables on the pixel/voxel representation of the microstructures, whereas our parametric homogenization focuses on the microstructures undergoing parametric shape modifications.

In summary, the main contributions of the study include the following aspects. First, the novel concept of a direct design-to-stress mapping is proposed that can instantly predict within any level of accuracy the stress distribution of a cellular structure under the design modifications. Second, a numerical approach to computing the mapping is developed by conducting an offline bi-scale parametric FE analysis using the solution in a reduced form as the sum of products of one-variable functions, which is built upon previous studies on PGD. Third, a particular numerical approach was devised to accelerate the PGD solution computation for such cellular structures under microstructural modifications, in combination with HOSVD. Fourth, various 2D and 3D numerical examples are tested to demonstrate the performance of the approach.

The remainder of this paper is arranged as follows. Related studies are first discussed in Section 2. The basics and problem of a direct design-to-stress mapping are described in Section 3. In addition, the overall numerical approach to resolving it is given in Section 4. The PGD approach used to compute the parametric mapping even in a varied domain is described in Section 5, along with further variable decomposition. Various 2D and 3D examples are provided in Section 6, and some concluding remarks are given in Section 7.

2. Related work

Designing cellular structures for a performance optimization dates to the seminar work of Olson (1997). Since then, researchers from different research communities have devoted significant effort to the topic, including those in the fields of computational materials, topology optimization, and computer graphics.

Descriptor-based design. Accelerating the process of novel material discovery is always a long-term goal in material research. Perhaps limited by the fabrication technologies of the time, researches have mainly focused on stochastic cellular structures, quantitatively described based on the stochastic distributions of the elements, such as a *first-order descriptor*, or *second-order descriptors* (Panchal et al., 2013). Using such descriptors, the material properties can then be predicted using analytical homogenization theory (Fullwood et al., 2010). Such studies have paved the way for novel material designs. However, the intrinsic statistical property is also a limit in terms of inaccurate geometric descriptions, and the physical property predictions are varied within an overly large range. Previously, most of these researches have mainly focused on the microstructure properties, and have not considered the macrostructures made from such properties. Recently, utilizing the material texture to super-performance structure has also attracted researchers' interest. For example, Liu and Shapiro (2017) have done a prominent work

on its usage to construct structures with anisotropy, and Xu et al. proposed an efficient approach to generate semi-regular structures for performance optimization (Xu et al., 2017b,a).

Topology optimization. Topology optimization aims to find the optimal solid–void material distribution within a design domain for a performance optimization under certain constraints. Initially, Bendsøe and Kikuchi proposed a homogenization-based approach (Bendsøe and Kikuchi, 1988), and later on density-based approaches became prevalent (Sigmund and Maute, 2013). These previous studies mainly focus on macro-structural design, and later, the design of microstructures meeting certain extreme physical properties, such as a negative Poisson's ratio, was studied using an inverse homogenization process (Sigmund, 1994; Wang and Bertoldi, 2012; Huang et al., 2015). Building on these studies, researchers started to find optimal cellular structures by simultaneously optimizing the topologies at both the macro- and micro-scales (Rodrigues et al., 2002; Panetta et al., 2015), where the microstructures may be homogeneously or heterogeneously distributed. These bi-scale topology optimization approaches involve repeated FE computations on the overall macro-structure and each micro-structure and are extremely computationally expensive. As a comparison, the proposed approach can instantly predict the elastic property of a cellular structure.

Fabrication-oriented design. Designing optimal cellular structures for additive manufacturing has also attracted various research interests from the area of computer graphics in recent years. This was first studied to balance the material usage and physical performance (Chen, 2007; Chen and Wang, 2008; Wang et al., 2013; Lu et al., 2014). Very recently, Panetta et al. (2015) and Schumacher et al. (2015) also developed approaches to control the elastic behavior of porous structures. In addition, Wu et al. built an optimal bone-like structure (Wu et al., 2018) using topology optimization approaches built on a GPU (Wu et al., 2016). Zhu et al. proposed a two-scale framework to optimize the overall structure and material distributions for achieving the best functional performance (Zhu et al., 2017). Chen et al. recently proposed a novel numerical coarsening approach to simulating inhomogeneous and non-linear elastic objects using discontinuous shape functions (Chen et al., 2018). A very interesting study on the evolution of a microstructure of minimized stress concentrations was also recently conducted by Panetta et al. (2017). These studies have produced various structures exhibiting an optimal physical performance but are not applicable for an instant simulation of cellular structures.

Interactive design and model reduction. Accelerating the simulations used for visual effects is one of the most important topics in the field of graphics, and numerous excellent studies have been conducted, including the areas of garment editing (Umetani et al., 2011), fluid simulations (Treuille et al., 2006), large deformations (Barbič and Zhao, 2011), elastic motion (Li et al., 2014), material designs (Xu et al., 2015), and stress analysis (Chen et al., 2017). To the best of our knowledge, no studies have been conducted on interactive simulations for cellular structures thus far.

These previous approaches have mainly been achieved based on classical model reduction techniques (Barbič, 2012; Białecki et al., 2005; Ganapathysubramanian and Zabaras, 2007). However, applying such techniques for an instant simulation at any degree of accuracy control is extremely difficult. The first reason for this lies in the well-known curse of dimensionality. Consider for example a design space with ten design variables, each sampled ten times. The total number of samples in the space is 10^{10}. Its associated stress distribution is far too complex to compute in advance. For example, it was reported by Kim et al. that a limited spatial exploration of the detailed clothing effects on a character costs several thousand CPU hours (Kim et al., 2013).

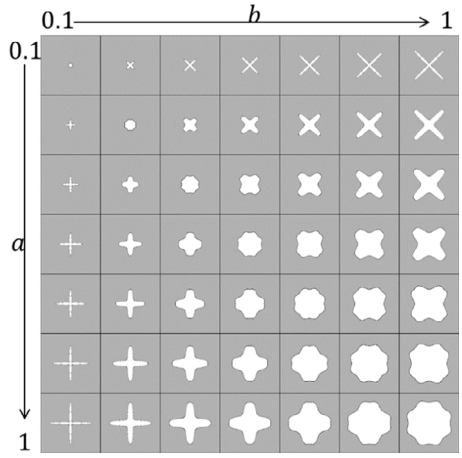

Fig. 3. Microstructures defined using implicit superformula in Eq. (1) at different shape controlling parameter values a, b when $l = 8$, $n_1 = n_2 = n_3 = 3$, and $w = 0.4$.

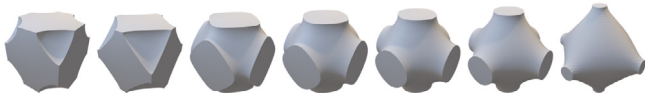

Fig. 4. Microstructures defined using implicit TPMS in Eq. (2) at different shape controlling parameter values C, namely, -1.5 to 0.9 in steps of 0.4 from left to right.

Next, a simulation based on a model reduction is conducted online in a low-dimensional space, and is unable to achieve both an instant simulation and high accuracy. Differing from this, the computed mapping can be controlled within any level of simulation accuracy, and the simulation of a specific case can be instantly predicted through a simple functional evaluation.

In order to overcome these limitations, Schulz et al. (2017) recently proposed an excellent approach to reduce the number of samplings based on an adaptive K-d tree grid. The stress field for specific instances can then be obtained through a smooth interpolation. The approach demonstrates nice performance at small number of design variables (maximally 6), but its extensions to more complicated case of larger number of design variables need to be further explored.

3. Basics and problem

The direct design-to-simulation mapping aims to establish a stress function in terms of the design variables, including the shapes of the microstructures, their distributions, and the magnitude of the external loadings. Some of the basics are first introduced, and the problem is then mathematically formulated.

3.1. Microstructures and their distributions

The types of microstructures and their overall distributions within a macrostructure are first described in sequence.

3.1.1. Microstructures

Various types of 2D or 3D microstructures represented as mesh models, or in parametric or implicit form, are studied here. In particular, we take three typical types of microstructures: the microstructures from Materialise Magics, an implicit superformula (Gielis, 2003), and an implicit 3D triply periodic minimal surface (TPMS), as shown in Figs. 2, 3, 4, and detailed below.

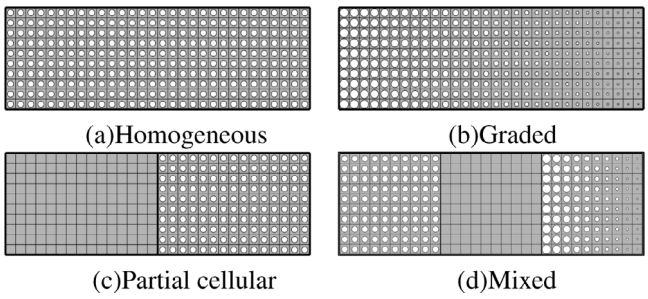

Fig. 5. Different types of microstructure distributions can be dealt with using our approach, which covers various design cases.

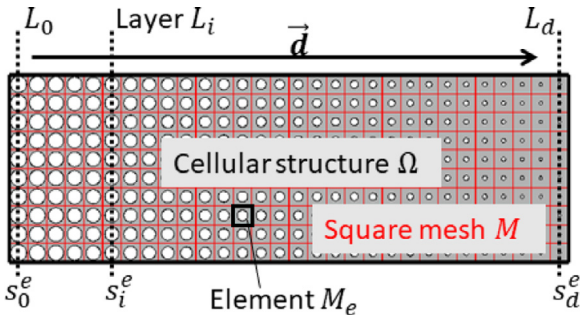

Fig. 6. A cellular structure Ω consisting of graded microstructures whose shape parameter varies from s_0^e to s_d^e with graded direction $\vec{d}$.

The implicit superformula is able to represent various types of closed 2D or 3D holes. In a 2D case, it has the following form:

$$\Phi(r,\phi,a,b,\theta) = \frac{1}{w}\cdot\left[\left|\frac{1}{a}\cos\left(\frac{l}{4}(\phi+\theta)\right)\right|^{n_2}+\left|\frac{1}{b}\sin\left(\frac{l}{4}(\phi+\theta)\right)\right|^{n_3}\right]^{\frac{1}{n_1}}-\frac{1}{r}, \quad (1)$$

where r, ϕ are polar coordinates satisfying $\phi \in [-\pi, \pi]$, $r\cos\phi \in [0, 1]$, and $r\sin\phi \in [0, 1]$; w is a constant to control the hole size; and a, b, θ are the shape controlling parameters. Fig. 3 shows the shapes for varying a, b when $l = 8$, $n_1 = n_2 = n_3 = 3$, and $w = 0.4$.

The classical 3D TPMS has the superior properties of an interior connection and zero mean curvature. In particular, we take the P-type element as described below:

$$\Phi(\mathbf{x}, C) = \cos(2\pi x-\pi)+\cos(2\pi y-\pi)+\cos(2\pi z-\pi)-C, \quad x,y,z\in[0,1]. \quad (2)$$

Its associated shapes with a varying C are shown in Fig. 4.

3.1.2. Microstructure distributions

Generalized functional graded microstructures (GFGM) are also included in this study, which includes microstructures distributed homogeneously or graded along certain directions, or partially solid, as indicated in Fig. 5.

We further explain the details of controlling the shapes of microstructures within the macro domain. Without loss of generality, let Ω be a 2D cellular structure under study, and M be its associated square mesh of element M_e; see also Fig. 6. Given a graded direction $\vec{d}$ and the starting locations, a set of layers L_i, $0 \le i \le d$ can be defined. Suppose $\mathbf{s}^e$ is a shape parameter describing a microstructure, and $\mathbf{s}_0^e, \mathbf{s}_d^e$ are the values of the parameter at the starting and end layers L_0, L_d, respectively. The shape parameter $\mathbf{s}_i^e$ for microstructure layer L_i can be defined using various interpolation techniques, and simply takes the following linear interpolation:

$$\mathbf{s}_i^e = \mathbf{s}_0^e + \frac{i}{d}(\mathbf{s}_d^e - \mathbf{s}_0^e). \quad (3)$$

$\mathbf{s} = (\mathbf{s}_0^e, \mathbf{s}_d^e)$ is treated as the shape controlling parameter for the whole structure here. It is explicit defined and is in accord with the user's instinct. In this case, for example, one can lower the value of $\mathbf{s}_0^e$ to make the left side of the cellular structure has the higher density, or get a homogeneous cellular structure by making $\mathbf{s}_0^e$ and $\mathbf{s}_d^e$ equal. In addition, the definitions can also be extended for part of an input model Ω.

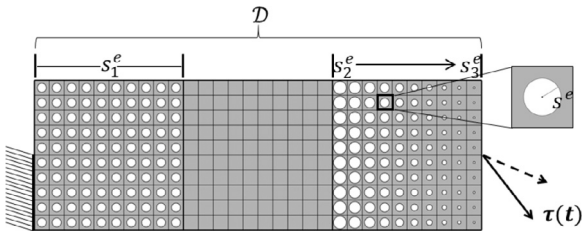

Fig. 7. A cellular structure constructed using various prescribed microstructure distributions.

3.2. Mathematical problem formulation

As illustrated in Fig. 7, the following notations are used throughout the paper.
Ω: a macro-structure, of fixed boundary Γ_D and loading boundary Γ_N under external loading $\boldsymbol{\tau}(\mathbf{t})$ of parameter $\mathbf{t} \in I_\mathbf{t}$;
M: the associated quadrilateral (for 2D) or hexahedral (for 3D) mesh to Ω;
$\omega(\mathbf{s}^e)$: a library of microstructures fixed or varied under parameter $\mathbf{s}^e \in I_\mathbf{s}$;
$\mathbf{s}(\mathcal{D})$: microstructures shape controlling parameter within M according to the microstructures distribution $\mathcal{D}$, or $\mathbf{s}$ for short;
$\Omega(\mathbf{s}(\mathcal{D}), \mathbf{t})$: cellular structure generated by embedding the microstructures $\omega(\mathbf{s})$ under distributions $\mathcal{D}$ for model Ω at load parameter $\mathbf{t}$.

For example in Fig. 7, while the middle 10×10 elements are solid, the left 10×10 microstructures are homogeneously distributed under the shape parameter $\mathbf{s}_1^e$ and the right 10×10 microstructures are horizontally graded distributed, where the shape parameter is changing from $\mathbf{s}_2^e$ to $\mathbf{s}_3^e$. We correspondingly have the shape controlling parameter for the whole cellular structure as $\mathbf{s} = (\mathbf{s}_1^e, \mathbf{s}_2^e, \mathbf{s}_3^e)$.

Using the above notations, the direct design-to-stress mapping aims to produce offline a stress mapping $\boldsymbol{\sigma}(\mathbf{x}, \mathbf{s}, \mathbf{t})$, or $\boldsymbol{\sigma}(\mathbf{s}, \mathbf{t})$ for short, under any level of accuracy control; for an illustration, see Fig. 1. Under this stress map, achieving an instant simulation of a prescribed cellular structure $\Omega(\mathbf{s}_0, \mathbf{t}_0)$ is as simple as evaluating $\boldsymbol{\sigma}(\mathbf{s}, \mathbf{t})$ at parameter $\mathbf{s}_0, \mathbf{t}_0$.

Accordingly, the mapping $\boldsymbol{\sigma}(\mathbf{s}, \mathbf{t})$ is determined based on the following high-dimensional simulation problem: Find displacement $\mathbf{u}$ such that

$$\begin{cases} -\mathrm{div}\boldsymbol{\sigma}(\mathbf{u}(\mathbf{x},\mathbf{s},\mathbf{t})) = \mathbf{f}, & \text{in } \Omega\times I_\mathbf{s}\times I_\mathbf{t},\\ \boldsymbol{\sigma}(\mathbf{u}(\mathbf{x},\mathbf{s},\mathbf{t}))\cdot\mathbf{n} = \boldsymbol{\tau}(\mathbf{t}), & \text{on } \Gamma_N,\\ \mathbf{u}(\mathbf{x},\mathbf{s},\mathbf{t}) = \mathbf{u}_D, & \text{on } \Gamma_D, \end{cases} \quad (4)$$

where $\mathbf{f}$ is the body force, and

$$\boldsymbol{\sigma}(\mathbf{s},\mathbf{t}) = \mathbf{C}\boldsymbol{\varepsilon}(\mathbf{u}(\mathbf{s},\mathbf{t})), \quad \boldsymbol{\varepsilon}(\mathbf{u}(\mathbf{s},\mathbf{t})) = \nabla_\mathbf{x}\mathbf{u}(\mathbf{s},\mathbf{t}),$$

for the fourth-order stiffness tensor $\mathbf{C}$.

Such mapping can also be constructed for cellular structures consisting of microstructures without parametric deformation. In

this case, the shape controlling parameter $\mathbf{s}$ is replaced by the coefficients of the elasticity tensor $\mathbf{C}$. The design-to-stress mapping with microstructures with or without parametric deformation can be obtained similarly following the approach explained later via the stiffness tensor being the design variable instead of $\mathbf{s}$.

3.3. Homogenization theory

It is prohibitively expensive for exact analysis of such bi-scale problems. The numerical homogenization theory (Bendsøe and Kikuchi, 1988; Andreassen and Andreasen, 2014) is adopted here for connecting the micro- and macro-scales, based on which our approach is proposed. The basic concept of numerical homogenization is therefore first described in this section.

The homogenization theory assumes that the size of the unit-cell M_e containing the microstructure ω is much smaller than the size of the macrostructure and the microstructure is periodically repeated throughout the macro-domain. Then the effective elasticity tensor of the periodic microstructure can be computed as:

$$(\mathbf{C}^H_\omega)_{ijkl} = \frac{1}{|M_e|}\int_\omega \mathbf{C}_{pqrs}(\boldsymbol{\varepsilon}^{0(ij)}_{pq} - \boldsymbol{\varepsilon}^{(ij)}_{pq})(\boldsymbol{\varepsilon}^{0(kl)}_{rs} - \boldsymbol{\varepsilon}^{(kl)}_{rs})\, dV, \tag{5}$$

where $|M_e|$ is the volume of the unit-cell M_e, $\mathbf{C}$ is elasticity tensor of the base material of which the microstructure is made, $\boldsymbol{\varepsilon}^{0(ij)}_{pq}$ are prescribed macroscopic strain fields, and $\boldsymbol{\varepsilon}^{(kl)} = \nabla_{\mathbf{x}}\boldsymbol{\mu}^{kl}$ are strain fields based on the displacement fields $\boldsymbol{\mu}^{kl}$ found by solving the elasticity equations

$$\int_\omega \mathbf{C}_{ijpq}\boldsymbol{\varepsilon}_{ij}(v)\boldsymbol{\varepsilon}_{pq}(\boldsymbol{\mu}^{kl})\, dV = \int_\omega \mathbf{C}_{ijpq}\boldsymbol{\varepsilon}_{ij}(v)\boldsymbol{\varepsilon}^{0(kl)}_{pq}\, dV \tag{6}$$

with the periodic boundary condition for an arbitrary virtual micro-displacement v. One may refer to Andreassen and Andreasen (2014) for more details.

4. Overall approach

Given a cellular structure $\Omega(\mathbf{s}(\mathcal{D}), \mathbf{t})$, the direct design-to-stress mapping $\boldsymbol{\sigma}(\mathbf{x}, \mathbf{s}(\mathcal{D}), \mathbf{t})$ is derived by computing the solution to the elasticity problem in Eq. (4) in the high-dimensional space $\Omega \times I_{\mathbf{s}} \times I_{\mathbf{t}}$. Owning to the intrinsic bi-scale geometrical structure of the cellular models, the solution is derived within a bi-scale FE analysis framework, where the two scales are linked through the homogenized elasticity tensors. The overall approach is first described below.

Parametric homogenization. First, for each microstructure $\omega(\mathbf{s}^e)$ (in the unit cell M_e) whose shape is controlled by parameter $\mathbf{s}^e$, $\mathbf{s}^e \in I_{\mathbf{s}^e}$, compute its associated parametric homogenized elasticity tensor

$$\mathbf{C}^H_{M_e} = \mathbf{C}^H_\omega = \mathbf{C}^H_\omega(\mathbf{s}^e). \tag{7}$$

It is achieved via the parametric homogenization procedure, based on the numerical homogenization theory, first computing the parametric displacement fields $\mu(\mathbf{s}^e)$ by solving the high-dimensional elasticity equations

$$\int_{\omega(\mathbf{s}^e)} \mathbf{C}_{ijpq}\boldsymbol{\varepsilon}_{ij}(v)\boldsymbol{\varepsilon}_{pq}(\boldsymbol{\mu}^{kl}(\mathbf{s}^e))\, dV = \int_{\omega(\mathbf{s}^e)} \mathbf{C}_{ijpq}\boldsymbol{\varepsilon}_{ij}(v)\boldsymbol{\varepsilon}^{0(kl)}_{pq}\, dV, \tag{8}$$

and then deriving the elasticity tensor from Eq. (5).

Design-to-stress mapping. Second, computing the design-to-stress mapping is equivalent to computing the numerical solution $\mathbf{u}(\mathbf{x}, \mathbf{s}(\mathcal{D}), \mathbf{t})$ to Eq. (4) in the parameter domain $\Omega \times I_{\mathbf{s}} \times I_{\mathbf{t}}$.

For the cellular structure Ω consisting of microstructures with parametric deformation, the shapes of the microstructures within the cellular structure are functions of the location and the shape controlling parameter $\mathbf{s}$ like Eq. (3), that is,

$$\mathbf{s}^e = \mathbf{s}^e(\mathbf{x}, \mathbf{s}). \tag{9}$$

With Eqs. (9), (7), we have the elasticity tensor being the function of the shape controlling parameter as $\mathbf{C} = \mathbf{C}^H(\mathbf{x}, \mathbf{s})$. And for the cellular structure consisting of microstructures without parametric deformation, the vector of coefficients of $\mathbf{C}$ is treated as the design domain instead of $\mathbf{s}$. And the mapping is constructed similarly.

Online evaluation. Once the distribution is modified ($\mathbf{s}$ is determined) and the magnitude of the external loadings is determined, we have the macro-scale displacement field $\mathbf{u}(\mathbf{s}, \mathbf{t})$ interactively by substituting the parameters $\mathbf{s}, \mathbf{t}$ into the parametric solution from the above design-to-stress mapping result. Ultimately, the stress is established by

$$\boldsymbol{\sigma} = \mathbf{C}^H(\mathbf{x}, \mathbf{s}) \cdot \nabla\mathbf{u}(\mathbf{x}, \mathbf{s}, \mathbf{t}).$$

However, solving the high-dimensional elasticity problems in Eqs. (8), (4) is still challenging because of the *curse of dimensionality*. This problem is resolved via the PGD approach here. Further details on the basics of the PGD, and our approach for extending it to domain of varying shape in a bi-scale simulation framework, are next explained.

5. PGD on domain of varied shape and further variable decomposition

PGD is a novel model reduction approach firstly introduced in Ammar et al. (2006, 2007), and aims to compute a simulation solution in the form of the sum of the products of one-variable functions (usually constructed on an FE basis). The solution can be computed within any level of accuracy control. Herein, we extend the usage of PGD to a varied design domain, and propose a novel approach based on a higher-order SVD to accelerate its computation. The basics on PGD is first explained in Section 5.1. The numerical approach, via an enrichment strategy with an embedded fixed-pointed iteration approach, to computing the PGD solution is then explained in Section 5.2. The details of the proposed approaches for parametric homogenization is then given in Section 5.3.

5.1. Basics on PGD

The basics of PGD are introduced below. PGD aims to compute to the high-dimensional problem similar to Eq. (4) as a parametric solution that possesses the form of the sum of the products of single variable functions. Let $\mathbf{p} = (p_1, \ldots, p_m) \in I_{\mathbf{p}}$ be a general parameter for the simulation problem in addition to the spatial coordinates $\mathbf{x}$. For example, $\mathbf{p} = \mathbf{s}^e$ for the parametric homogenization problem, or $\mathbf{p} = (\mathbf{s}, \mathbf{t})$ for the design-to-stress mapping in (4). We then have an approximated parametric solution in the following form:

$$\mathbf{u}(\mathbf{x}, \mathbf{p}) \approx \mathbf{u}^N(\mathbf{x}, \mathbf{p}) = \sum_{i=1}^{N} \mathbf{w}^i(\mathbf{x}) \prod_{j=1}^{m} q^i_j(p_j), \tag{10}$$

where $\mathbf{w}^i$ and q^i_j are functions in terms of the spatial coordinate vector $\mathbf{x} \in \mathbb{R}^2$ or $\mathbb{R}^3$ and extra parameter p_j, respectively, as represented by 3D and 1D FE bases and coefficients. It has been proven that $\mathbf{u}(\mathbf{x}, \mathbf{p})$ can be approximated within any degree of accuracy by $\mathbf{u}^N(\mathbf{x}, \mathbf{p})$ with a sufficient number of terms N (Chinesta et al., 2011a).

Determining the coefficients of functions $\mathbf{w}^i$ and q^i_j is similar to that of the classical FE method, but in a higher dimensional

space as $\Omega \times I_{\mathbf{p}}$. Specifically, it is computed as a solution $\mathbf{u}$ to the following variational problem derived from the simulation problem, for example Eq. (4): find $\mathbf{u}$ for all $\delta\mathbf{u}$ being the test function of $\mathbf{u}$ in the appropriate space such that

$$A(\mathbf{u}, \delta\mathbf{u}) = L(\delta\mathbf{u}), \tag{11}$$

where

$$A(\mathbf{u}, \delta\mathbf{u}) = \int_{I_{\mathbf{p}}} \int_{\Omega} (\nabla\mathbf{u})^T \mathbf{C} \nabla\delta\mathbf{u} \, d\Omega \, d\mathbf{p},$$
$$L(\delta\mathbf{u}) = \int_{I_{\mathbf{p}}} \left(\int_{\Omega} \mathbf{f}^T \delta\mathbf{u} \, d\Omega + \int_{\Gamma_N} \boldsymbol{\tau}^T \delta\mathbf{u} \, dS \right) d\mathbf{p}.$$

5.2. Numerical approach to computing PGD

Algorithm 1 Numerical approach for PGD

1: **Initialize** Set the solution $\mathbf{u} = \mathbf{0}$, the enrichment step N=0, and the approximation error *err_iter*=1, and provide the maximal enrichment step *max_enrich*, the maximal iteration step *max_iter*, and the tolerance error *tol*.
2: **while** *err_iter* $>$ *tol* and $N <$ *max_enrich* **do** // Enrichment loop
3: $N = N + 1$
4: **Initialize** Set $\mathbf{w} = \mathbf{0}$, $q_j = \mathbf{1}$, $j = 1, \cdots, m$, the error $err = 1$, and the iteration step $n = 0$.
5: **while** *err* $>$ *tol* and $n <$ *max_iter* **do** // Fixed-point loop
6: $n = n + 1$ //Increase the iteration step.
7: $\mathbf{w}^d = \mathbf{w}$, $q_j^d = q_j$, $j = 1, \cdots, m$ // Record the origin values for a fixed point check.
8: Find $\mathbf{w}$ for all $\delta\mathbf{w}$ such that
$$A(\mathbf{w}\prod_{j=1}^{m} q_j) = L(\delta\mathbf{w}\prod_{j=1}^{m} q_j) - A(\mathbf{u}^{N-1}, \delta\mathbf{w}\prod_{j=1}^{m} q_j).$$
9: Find q_k $(k = 1, \cdots, m)$ one by one for all corresponding δq_k such that
$$A(\mathbf{w}\prod_{j=1}^{m} q_j) = L(\mathbf{w}\delta q_k \prod_{j\neq k} q_j) - A(\mathbf{u}^{N-1}, \mathbf{w}\delta q_k \prod_{j\neq k} q_j).$$
10: $err = ||\mathbf{w}^d - \mathbf{w}|| + \sum_{j=1}^{m} ||q_j^d - q_j||$ //Check whether the fixed point has been reached.
11: **end while**
12: $\mathbf{u} = \mathbf{u} + \mathbf{w}\prod_{j=1}^{m} q_j$. // Enrich the solution.
13: $err\_iter = ||\mathbf{w}|| \cdot \prod_{j=1}^{m} ||q_j||$ // Check whether the solution has reached convergence.
14: **end while**
15: **Return u**.

The numerical approach to solving the highly nonlinear equation Eq. (11) consists of a greedy enrichment procedure with an iterative fixed-point procedure, as briefly described in Algorithm 1 and explained below. For further details, refer to Ammar et al. (2006, 2007).

The number of terms increases by 1 after each enrichment step. Specifically, supposing that $\mathbf{u}^{i-1}(\mathbf{x}, \mathbf{p})$ is already known, after the $(i-1)$th enrichment step, we then enrich the solution in the following form:

$$\mathbf{u}^i(\mathbf{x}, \mathbf{p}) = \mathbf{u}^{i-1}(\mathbf{x}, \mathbf{p}) + \mathbf{w}(\mathbf{x}) \prod_{j=1}^{m} q_j(p_j), \tag{12}$$

where $\mathbf{w}(\mathbf{x})$ and $q_j(s_j)$ $(j = 1, \ldots, m)$ are functions to be determined in the ith enrichment through the following procedure.

Substituting Eq. (12) into Eq. (11) provides

$$A(\mathbf{w}\prod_{j=1}^{m} q_j, \delta\mathbf{u}) = L(\delta\mathbf{u}) - A(\mathbf{u}^{i-1}, \delta\mathbf{u}). \tag{13}$$

An iterative fixed-point procedure is applied to compute $\mathbf{w}$ and q_j, $j = 1, \ldots, m$, one by one, by fixing the other functions. In this process, the test function $\delta\mathbf{u}$ is chosen as the following separated form:

$$\delta\mathbf{u} = \delta\mathbf{w}\prod_{j=1}^{m} q_j + \sum_{k=1}^{m} \mathbf{w}\delta q_k \prod_{j=1, j\neq k}^{m} q_j, \tag{14}$$

where $\delta\mathbf{w} \in \{\mathbf{w} | \mathbf{w} \in \mathcal{H}^1(\Omega), \ \mathbf{w} = 0 \text{ on } \Gamma_D\}$, and $\delta q_k \in \mathcal{L}^2(I_k)$ are chosen as the FE basis function associated with each FE grid in its own space.

Note it is also well known that the convergence of the fixed-point algorithm is not guaranteed, but generally provides good results (Cueto et al., 2016). Once the fixed-point iterations solve for the optimal rank 1 enrichment term and using the optimal enrichment term at each step is sufficient to guarantee convergence with a sufficient number of terms (Falcó and Nouy, 2011; Chinesta et al., 2011a). The accuracy and convergence of PGD, and its ability in resolving curse of dimensionality will be further discussed in Section 6.4.

5.3. PGD over parametric domain

Previous studies on PGD have mainly focused on a fixed or simple parametric domain. Its extension to a varied parametric domain is systematically described in this section. In particular, a strategy based on HOSVD that greatly accelerates its computation is proposed. We specifically explain the procedure for computing the PGD solution to the homogenization equation in Eq. (6).

5.3.1. Domain transformation

With this situation, the microstructure ω involved in Eq. (6) varies under the design parameter $\mathbf{s}^e \in I_{\mathbf{s}^e}$. We first transform the parameter $\mathbf{s}^e$ to that in the integration function using a characteristic function in the integration function.

Specifically, given a varying shape $\omega(\mathbf{s}^e)$, $\mathbf{s}^e \in I_{\mathbf{s}^e}$, in the micro structure cell M_e (a square in a 2D problem, or a cube in a 3D problem), the boundary of $\omega(\mathbf{s}^e)$ is defined by $\Phi : M_e \times I_{\mathbf{s}^e} \to \mathbb{R}$ such that

$$\begin{cases} \Phi(\mathbf{x}, \mathbf{s}^e) > 0, & \mathbf{x} \text{ inside } \omega(\mathbf{s}^e), \\ \Phi(\mathbf{x}, \mathbf{s}^e) = 0, & \mathbf{x} \text{ on the boundary of } \omega(\mathbf{s}^e), \\ \Phi(\mathbf{x}, \mathbf{s}^e) < 0, & \mathbf{x} \text{ outside } \omega(\mathbf{s}^e). \end{cases} \tag{15}$$

We also define the following characteristic function,

$$H(\Phi(\mathbf{x}, \mathbf{s}^e)) = \begin{cases} 1, & \text{if } \Phi(\mathbf{x}, \mathbf{s}^e) \geq 0, \\ 0, & \text{if } \Phi(\mathbf{x}, \mathbf{s}^e) < 0, \end{cases} \tag{16}$$

which indicates whether a given point $\mathbf{x}$ belongs to $\omega(\mathbf{s}^e)$.

Accordingly, from Eq. (6) we have

$$\begin{aligned} &\int_{I_{\mathbf{s}^e}} \int_{M_e} H \cdot \mathbf{C}_{ijpq} \boldsymbol{\varepsilon}_{ij}(v) \boldsymbol{\varepsilon}_{pq}(\boldsymbol{\mu}^{kl}(\mathbf{s}^e)) \, dV d\mathbf{s}^e \\ &= \int_{I_{\mathbf{s}^e}} \int_{M_e} H \cdot \mathbf{C}_{ijpq} \boldsymbol{\varepsilon}_{ij}(v) \boldsymbol{\varepsilon}_{pq}^{0(kl)} \, dV d\mathbf{s}^e, \end{aligned} \tag{17}$$

where $\mathbf{C}$ is a constant in M_e, being the elasticity tensor of the base material for the microstructures, and the parametric solution $\boldsymbol{\mu}^{kl}(\mathbf{s}^e)$ can be solved in the separated form using PGD.

5.3.2. High-order SVD for function separation

The expression in Eq. (17) provides a simulation problem defined in the fixed domain M_e. Note that $\mathbf{s}^e = (s_1^e, \ldots, s_r^e)$ is the design parameter of the micro-structures, and $I_{\mathbf{s}^e} = \prod_{j=1}^{r} I_{s_j^e}$. However, the characteristic function $H(\Phi(\mathbf{x}, \mathbf{s}^e))$ is not separated in its variables $s_1^e, \ldots, s_r^e$, which prohibits an efficient integration.

This is to be resolved by approximating $H(\Phi(\mathbf{x}, \mathbf{s}))$ using a function as the sum of one-variable functions based on the concept of HOSVD (Kolda and Bader, 2009). HOSVD decomposes a tensor into a core tensor multiplied by a factor matrix along each mode, which is used to approximate the function following a sampling, tensor decomposition, and variable separation procedure.

1. Sampling. Obtain a $n_x \times n_y \times \cdots \times n_{s_r}$ grid mesh for the high-dimensional domain $M_e \times I_{\mathbf{s}^e}$ and sample the values of the characteristic function H at the grid points $(x_{i_x}, y_{i_y}, z_{i_z}, s_{1_{i_{s1}}}, \ldots, s_{r_{i_{sr}}})$ to obtain the tensor $\mathcal{H} \in \mathbb{R}^{n_x \times n_y \times n_z \times n_{s_1} \times \cdots \times n_{s_r}}$:

$$\mathcal{H}_{i_x, i_y, i_z, i_{s1}, \ldots, i_{sr}} = H(x_{i_x}, y_{i_y}, z_{i_z}, s_{1_{i_{s1}}}, \ldots, s_{r_{i_{sr}}}), \quad i_* = 1, \ldots, n_*$$

2. Tensor decomposition. HO-SVD is applied (Bader et al., 0000) to the tensor $\mathcal{H}$, obtaining

$$\overline{\mathcal{H}} = \mathcal{S} \times_1 U^x \times_2 U^y \times_3 U^z \times_4 U^{s_1} \times_5 \cdots \times_{r+3} U^{s_r},$$

where $\mathcal{S}$ is the core of size $\overline{n}_x \times \overline{n}_y \times \cdots \times \overline{n}_{s_r}$, each $U^* \in \mathbb{R}^{n_* \times \overline{n}_*}$ is a factor matrix corresponding to dimension $*$, and $\times_k$ indicates the k-mode product of the tensors. $\overline{\mathcal{H}}$ is an approximation of $\mathcal{H}$ with accuracy control by choosing $\overline{n}_x, \overline{n}_y, \ldots, \overline{n}_{s_r}$ $(1 \le \overline{n}_* \le n_*)$ satisfying $\|\mathcal{H} - \overline{\mathcal{H}}\| < \epsilon$, where ϵ is the tolerance.

3. Variables separation. Using the columns of the factor matrices as a coefficient vector to construct the interpolate functions, the characteristic function $H(\mathbf{x}, \mathbf{s})$ can be decomposed as follows:

$$H \approx \sum_{i_x=1}^{\overline{n}_x} \cdots \sum_{i_{sr}=1}^{\overline{n}_{sr}} \mathcal{S}_{i_x, \ldots, i_{sr}} \overline{U}^x_{i_x}(x) \overline{U}^y_{i_y}(y) \overline{U}^z_{i_z}(z) \cdot \overline{U}^{s_1}_{i_{s1}}(s_1) \cdots \overline{U}^{s_r}_{i_{sr}}(s_r),$$

where each $\overline{U}^*_i$ is a function of $*$ represented by the coefficient vector U^*_i as the ith column of U^* and based on a 1D linear FE.

4. Integration computation. As a result, the variables are separated for the multivariable function $H(\mathbf{x}, \mathbf{s}^e)$, and the high-dimensional integration is approximated as the sum of the products of some low-dimensional integrations in the following form, which takes much less computational effort:

$$\begin{aligned} &\int_{I_{s_1^e}} \cdots \int_{I_{s_r^e}} \int_{M_e} H(\mathbf{x}, \mathbf{s}^e) \mathbf{z}(\mathbf{x}) \prod_{j=1}^{r} t_j(s_j^e)\, d\mathbf{x} ds_r^e \cdots ds_1^e \\ &\quad = \sum_{i_x=1}^{\overline{n}_x} \cdots \sum_{i_{sr}=1}^{\overline{n}_{sr}} \mathcal{S}_{i_x, \ldots, i_{sr}} \int_{\omega^U} \mathbf{z}(\mathbf{x}) \overline{U}^x_{i_x}(x) \overline{U}^y_{i_y}(y) \overline{U}^z_{i_z}(z)\, d\mathbf{x} \\ &\qquad \cdot \int_{I_{s_1}} t_1(s_1) \overline{U}^{s_1}_{i_{s1}}(s_1)\, ds_1 \cdot \cdots \cdot \int_{I_{s_r}} t_r(s_r) \overline{U}^{s_r}_{i_{sr}}(s_r)\, ds_r. \end{aligned} \tag{18}$$

where $\mathbf{z}$ and t_j are general functions of $\mathbf{x}$ and s_j respectively.

6. Experiments

The proposed approach to derive the direct design-to-stress mapping was implemented on a PC with a 3.6 GHz Intel Core i7 CPU and 32 GB of RAM. The performance was tested for various 2D and 3D structures. The 2D examples were mainly to evaluate the mapping accuracy and its computational costs, whereas the industrial 3D examples were mainly to demonstrate the performance on complex macro- and micro-structures. All materials used have a Young's modulus of 1 N/m^2 and a Poisson's ratio of 0.33. The unit cell is meshed to 10 × 10 in 2D case or a 10 × 10 × 10 in 3D case for microstructure homogenization. The approach computes once all the solutions for the design parameters within a certain range. In order to demonstrate its performance, the results obtained via classical FEA or numerical homogenization at a prescribed parameter are used as benchmark. In all the accuracy analysis, the accuracy measured does not consider the error from homogenization. Results on the numerical experiments are summarized in Table 1.

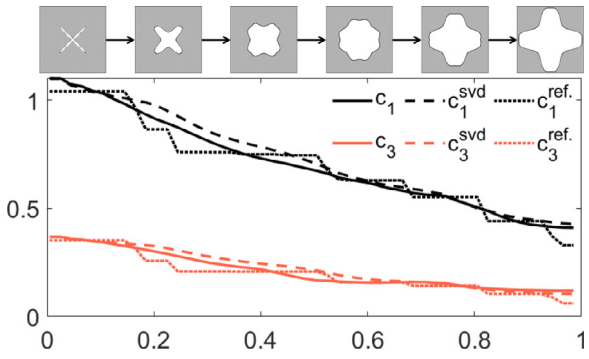

Fig. 8. Comparison between the components of the computed effective elasticity tensor mapping c_1, c_3 without HOSVD and c_1^{svd}, c_3^{svd} with HOSVD, and the benchmark traditional homogenization results $c_1^{ref.}, c_3^{ref.}$ at the sampling points. The microstructures are defined using the superformula in Eq. (1) under variation of the parameters a when $b = 0.6, \theta = 0$.

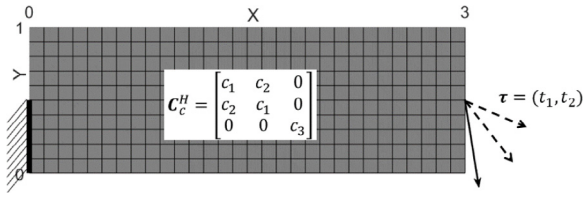

Fig. 9. Studied 2D beam-like example with varying material property and external loading parameters.

6.1. Accuracy analysis

The derived mapping can approximate the solution to the problem in Eq. (4) with high accuracy, which we first illustrate for various 2D design cases at both the micro- and macro-scales.

Microstructures. To evaluate the accuracy of the parametric homogenization approach, the microstructures described by the superformula in Eq. (1), and illustrated in Fig. 3, were first tested. In addition to the planar coordinates (x, y), there are three extra shape controlling parameters $a, b \in [0, 1]$, and $\theta \in [0, \pi]$. It takes about 1.1×10^4 s and 1.5×10^3 s to obtain a 15-term PGD solution of the homogenized elasticity tensor offline without and with the HOSVD, respectively. The results obtained are also compared with the benchmark results obtained using the FEA, sampled with a 20 × 20 mesh, shown in Fig. 8. The comparison among c_2, c_2^{svd}, and $c_2^{ref.}$ is omitted because c_2 and c_3, and c_2^{svd} and c_3^{svd}, are alike. In addition, c_1 and $c_1^{ref.}$ demonstrate a close approximation at a mean relative error of 1.4%, whereas c_1^{svd} and $c_1^{ref.}$ demonstrate a close approximation at a mean relative error of 5.0%.

Macro-structures. The simulation accuracy for a macro-structure was also studied on a 2D beam-like example, as shown in Fig. 9. For a clear explanation, the macro-structure is assumed to be made of orthotropic homogeneous microstructures, e.g. the superformula shapes with $\theta = 0$, whose elasticity tensor is controlled by parameters c_1, c_2, c_3 in the form of the 2D orthotropic property. In addition, the external loading exerted on the model $\boldsymbol{\tau}(t_1, t_2)$ is controlled using the parameters t_1, t_2.

Denoting $\overline{*} = */c_1$, we have a boundary value problem of the 4 design parameters $\overline{c_2}$, $\overline{c_3}$, $\overline{t_1}$, and $\overline{t_2}$. It takes 525 s to obtain an *offline* PGD solution of 200 ($N = 200$) separated terms. In Fig. 10 we compare the computed displacement or stress fields with the benchmark FE results for specific values of $c_1 = 10^3$, $\overline{c_2} = 0.5$, $\overline{c_3} = 0.2$, $\overline{t_1} = 0.5$, and $\overline{t_2} = -0.8$. The mean relative errors at different parameter values are also plotted in Fig. 11.

Table 1
Summary of execution time of the 2D and 3D examples studied.

Case	Mesh	Design variables	Grids per variable	Offline time	Online time	FEA time	Estimated brute-force sampling time
2D superformula	10 × 10	3	10	24.8 m (15 terms)	5.7 ms	1.0 s	22.2 m (11^3 samples)
Macro beam	300	4	10	525 s (200 terms)	5.8 ms	0.41 s	100 m (11^4 samples)
General cellular case	300	8	10	3.50 h (30 terms)	1.3 ms	0.85 s	5.06×10^4 h (11^8 samples)
Femur bone	12250	2	28	4.07 h (20 terms)	31 ms	6.8 s	1.59 h (29^2 samples)
Offset link	19417	3	15	1.10 h (15 terms)	37 ms	8.5 s	9.67 h (16^3 samples)

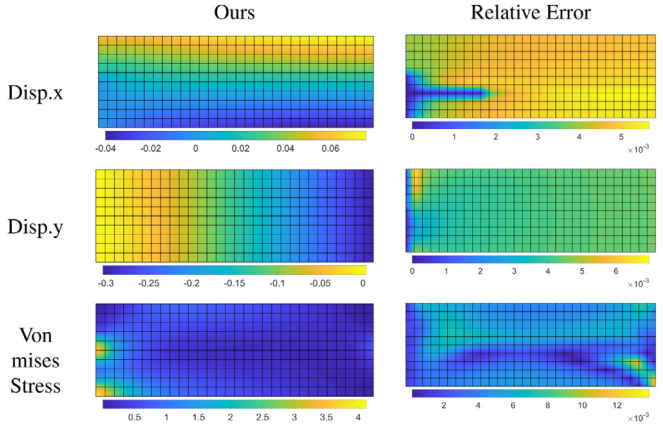

Fig. 10. Comparison of the macro simulation results obtained using the proposed approach against the benchmark FE results in the case of $c_1 = 10^3$, $\overline{c_2} = 0.5$, $\overline{c_3} = 0.2$, $\overline{t_1} = 0.5$, and $\overline{t_2} = -0.8$.

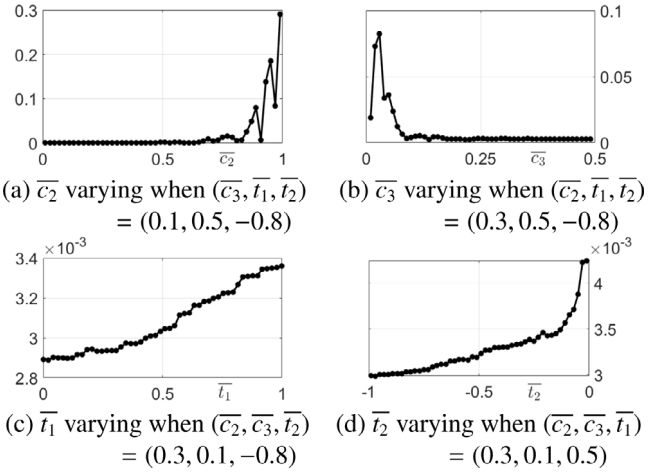

Fig. 11. Mean relative errors as the material parameters or loading parameters vary for the example shown in Fig. 9.

Accuracy control. Using the proposed approach, the stress mapping can be achieved within any simulation accuracy. In Fig. 12, the average relative error decreases as more PGD terms are computed, at the cost of an increase in the computational time. For example, we used 10 terms to achieve an approximation error of 3.9%, 50 terms for 0.7%, and 200 terms for 0.45%. We also notice that the relative error curve in Fig. 12 does not decrease monotonically but ends with a lower value, which may come from the fact that a maximal fixed-point iteration number is set in our implementation.

6.2. Performance on 2D cellular structure design

We further tested the performance of the approach on an overall cellular structure containing various microstructure distributions: homogeneous/partial/graded cellular structures. The

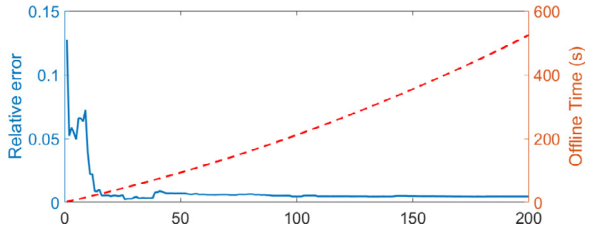

Fig. 12. As the number of PGD terms increases, the relative approximation decreases at the cost of an increase in the computational time for the case shown in Fig. 9 when $c_1 = 10^3$, $\overline{c_2} = 0.5$, $\overline{c_3} = 0.2$, $\overline{t_1} = 0.5$, and $\overline{t_2} = -0.8$.

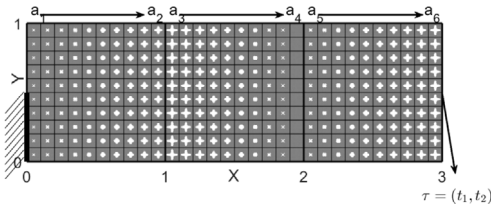

Fig. 13. A specific 2D example of cellular structures.

design-to-stress mapping is computed once for all general cases, and specific value settings provide different types of cellular structures.

The test was conducted on the cellular structure shown in Fig. 13, determined by applying six design parameters, namely, a_i, $i = 1, \ldots, 6$, the distribution control of the microstructures, and two other parameters t_1, t_2 controlling the external loading. The structure has three different cellular parts, each made of 10×10 superformula-shaped microstructures in which the a values controlled by the design parameters a_i, $i = 1, \ldots, 6$, and $b = 0.4, \theta = 0$ are constant (see also Eq. (1)). $a_1, \ldots, a_6$ are treated as extra parameters beyond the external force parameters t_1, t_2.

It takes approximately 3.50 h to get the design-to-stress mapping under accuracy control, which consists of a 30-term PGD solution with those 8 parameters. And it takes about 5.8 ms for a specific design online using our approach while it takes about 8.5 s using the straight-forward approach including computing the effective elasticity tensor of each microstructure via numerical homogenization and the FEA on the macro-model with the computed homogenized elasticity tensors. When $\mathbf{a} = (a_1, \ldots, a_6)$ take different values, the general case can be reduced to the case of a partial cellular structure, or graded cellular structure, as detailed below.

Partial cellular structures. When $a_1 = a_2 = \mathbf{a}_1^{\square}$, $a_3 = a_4 = \mathbf{a}_2^{\square}$, $a_5 = a_6 = \mathbf{a}_3^{\square}$, and at least one, but not all, of $\mathbf{a}_1^{\square}, \mathbf{a}_2^{\square}, \mathbf{a}_3^{\square}$ is zero, the general case is reduced to a partial cellular structure, as shown in Fig. 14(a),(c),(e). As can be seen from the results, different types of cellular structures provide very different simulation results.

Graded cellular structures. In this test, we set $a_2 - a_1 : a_3 - a_2 : a_4 - a_3 : a_5 - a_4 : a_6 - a_5 = 9 : 1 : 9 : 1 : 9$, which gives the graded cellular structure shown in Fig. 14(b). The values of a_1, a_6 are controlling parameters used to determine the microstructure

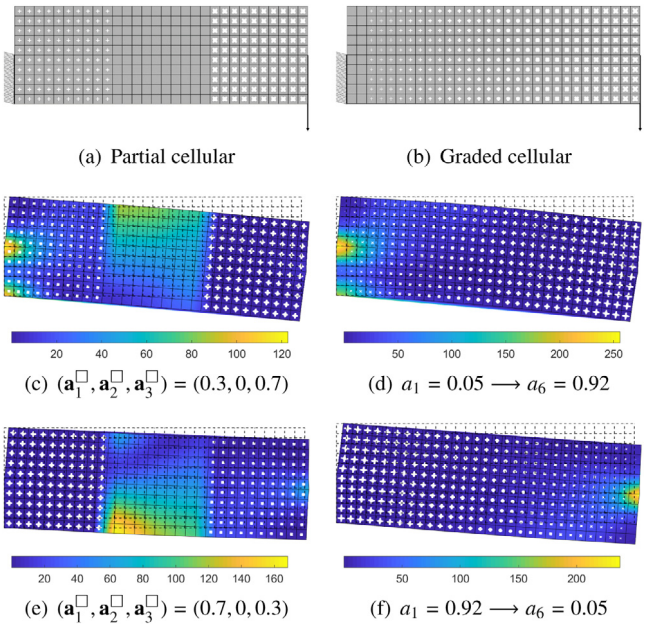

Fig. 14. The stress distribution for cellular structures of different microstructure distributions with different shape parameters can be instantly evaluated using the derived design-to-stress mapping for the cellular structure in Fig. 13. The external loadings for these figures are all the same as $\boldsymbol{\tau} = (0.5, -0.8)$. (The deformation in the figure is scaled by 10^{-2} for illustration.).

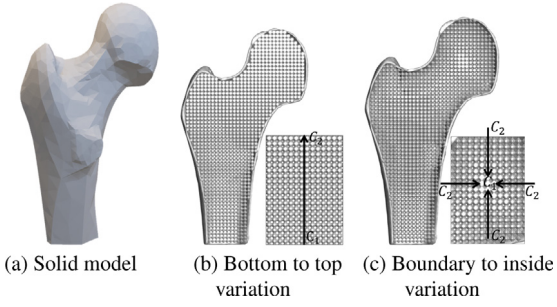

Fig. 15. Femur bone consisting of different gradually varied microstructures represented in TPMS defined using Eq. (2), where C_1, C_2 are the design parameters.

distributions. Once a_1, a_6 are given, the associated stress fields of the cellular structure were instantly derived. See for example the results in Fig. 14(d),(f) for two different cases: $a_1 = 0.05, a_6 = 0.92$, and $a_1 = 0.92, a_6 = 0.05$.

6.3. 3D cases

Various 3D examples were also tested to demonstrate the usage of the derived mapping in an instant simulation. This consists of a Femur bone in Fig. 15, an offset link with voxel meshes in Fig. 18. The simulation of a general hexahedral model has to take further account of the Jacobian matrix. The microstructures are generated using TPMS or models from Materialise Magics.

Femur bone. The femur bone in Fig. 15 consists of a gradual variation of TPMS cells within a shell, where the macro-structure has a voxel mesh of 12,250 elements and 14,960 nodes. Two different methods were used to control the distribution of the microstructures: changing from *boundary to inside* and from *bottom to top*, as shown in Fig. 15(b),(c), respectively. In each case, we used two shape parameters C_1, C_2 to define the microstructure distributions, from which the interior shapes are derived using

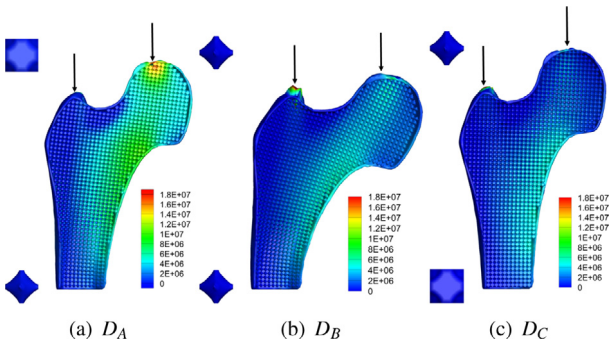

Fig. 16. The Von mises stress distributions and deformations (scaled) of different cellular designs depicted in Fig. 15(b) at different distribution of microstructures at parameters of $D_A = (0.9, -1.46)$, $D_B = (0.9, 0.9)$, $D_C = (-1.31, 0.9)$.

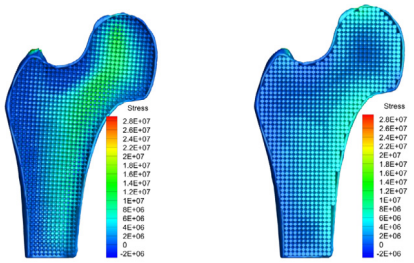

Fig. 17. The Von mises stress distributions and deformation (scaled) of the *boundary to inside* gradually vary the cellular bone structure in Fig. 15(c) with different microstructures distributions.

linear interpolation. Different values of C_1, C_2 provide different types of distributions. It takes approximately 4.07 h to compute the 20-term PGD solution offline using these 2 shape control parameters. Once the offline process is complete, the stress distribution of each design case can be instantly derived, which can take as short as 45 ms. The simulation results for the cases in Fig. 15(b),(c) are shown in Figs. 16, 17, respectively.

Offset link. The offset link model in Fig. 18 consists of two rings with a link between them. A voxel mesh of 19,417 elements and 24,147 nodes is generated for the macro model. We assume that the two rings are solid and that the link consists of homogeneous microstructures whose elasticity tensor is controlled by 3 material parameters for the orthotropic microstructures. It took approximately 1.10 h to obtain the PGD solution offline. After this, the macro-scale stress distribution an be instantly obtained for different microstructures. The associated results are respectively shown in Fig. 19 for TPMS microstructures and in Fig. 20 for the orthotropic microstructures from Materialise Magics.

6.4. Discussions

Curse of dimensionality. The proposed approach achieves the performance of instant stress prediction essentially via resolving the curse of dimensionality using PGD. It is mainly achieved via separating the variables following two main strategies, separating the variables both in the solution and in the integrands. Firstly, the solution to a high-dimensional problem is represented in the form of separated variables, as in Eq. (10). This is achieved by assuming that the parametric solution can be approximated using limited terms, each of which is the product of the functions of separated variables. Secondly, the integrands are further separated via separating the characteristic function of the parametric deforming geometric domain using HOSVD, whereas the

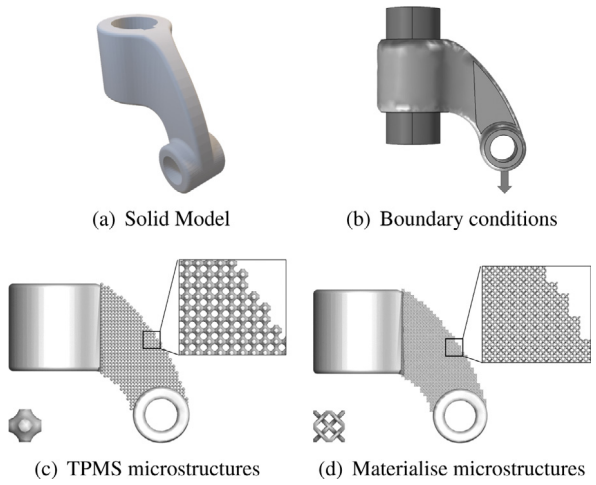

Fig. 18. A partial cellular offset link model consisting of different microstructures.

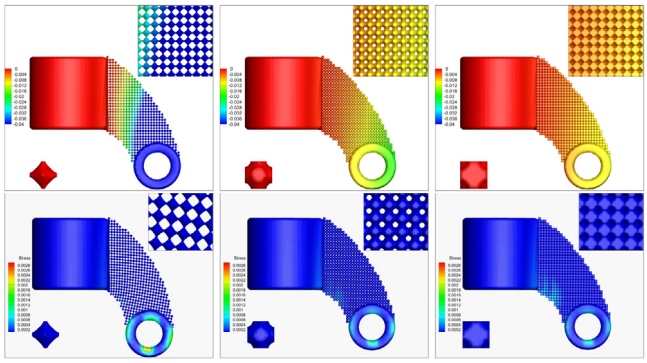

Fig. 19. Displacement fields (top row) and Von mises stress distributions (bottom row) of the cellular offset link structure consisting of different microstructures determined by different TPMS shape parameters defined using Eq. (2). The shape parameters are $C = 0.9, -0.26, -1.42$, respectively from left to right.

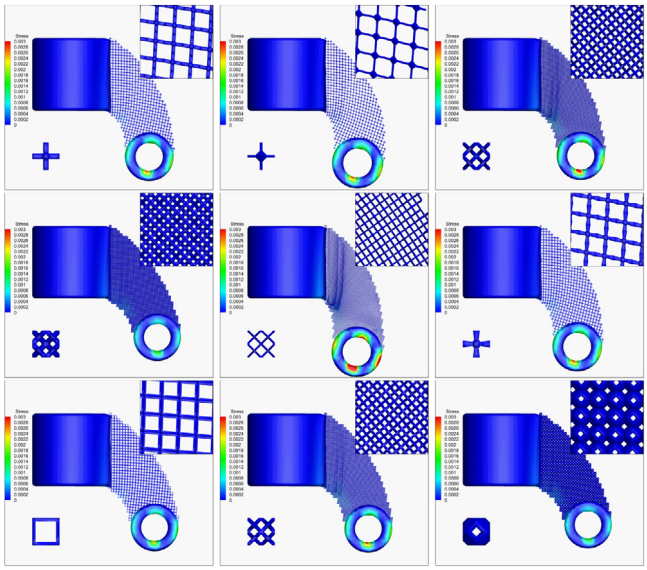

Fig. 20. Von mises stress distributions and deformations of the offset structures with 9 different microstructures from Materialise Magics. It takes about 37 ms to obtain the simulation results once the microstructure is determined or replaced.

material property and external force parameters in the integrand are naturally separated through a mathematical derivation. As a consequence, the integration involved in the process of stress computation, can be performed in each separable variable space. Ultimately, the computational complexity of the derived problem using our approach is far less than that of the original high-dimensional approach, and consequently avoids the issue of curse of dimension.

In practice, we found that the PGD result of less than 100 terms provides good results, e.g. the 16-term result gets an approximation error below 1% for the macro beam example in Section 6.1. Similar observations were also found in Chinesta et al. (2011a), where the authors found in all cases that the approximation converges towards its target solution, and show their confidence about the generality of the PGD. However, the number of terms required to obtain an accurate solution may depend on the regularity of the exact solution, instead of the problem dimension, as pointed out by the authors (Chinesta et al., 2011a) from their empirical observations. When an exact solution of a particular problem can be represented by a reduced number of functional products within enough accuracy, the PGD approximation is optimal. Otherwise, the solution is a non-separable function for the particular coordinate system used, and the number of terms in the PGD expansion does grow in order to span the full tensor basis of approximation functions. In this case, the PGD then offers no particular advantage , and the curse of dimensionality is not essentially resolved using PGD.

Accuracy and convergence. The design to stress mapping is computed via two main steps: determining the parametric material property for micro-structures using PGD in combination of HOSVD, and computing the parametric stress in terms of material properties and external loadings using PGD. Thus, the accuracy of the final design to stress mapping is determined by the numerical accuracy of PGD and HOSVD; the homogenization error is ignored in the study. In addition, the accuracy of the PGD approach is mainly affected by the strategy of fixed-point iterations and the enrichment strategy of adding more PGD terms, as seen from Algorithm 1. The algorithmic convergence is similarly determined.

In our experiments in Section 6.1, tens of enrichment steps provide a result of mean relative error below 5% for most parameter points. Specifically in the parametric homogenization process without using HOSVD, an accuracy at a mean relative error of 1.4% was obtained for the superformula case. Further applying HOSVD in the parametric homogenization will separate the variables and reduce the computation efforts, but on the other hand surely decreases the accuracy. Specifically in this example, applying HOSVD to approximate the characteristic function has an approximation error of 3.8% on the sampling grids. It in turn ultimately gives a mean relative error of 5% for the parametric homogenization with HOSVD.

It is also noticed that the stress we computed herein is homogenized because the micro- and macro-scales are linked by the homogenized elasticity tensor, and the specific geometric information of the micro-structures is lost in a certain sense. The pointwise stress inside the microstructure, which actually determines the structure fracture, may be higher depending on the geometry of the microstructure. As future work, we plan to look into a new multiscale framework such as FE^2, instead of homogenization, to capture the physical properties of the points inside the microstructure.

Offline computation complexity. The computational complexity is analyzed. Let $N_{\mathbf{x}}$ and N_{p_j} be number of degrees of freedom of the functions $\mathbf{w}^i(\mathbf{x})$ and q_j^i, in Eq. (10) respectively.

Using the PGD approach results in a computation problem of complexity

$$(N_{\mathbf{x}} + \sum_{j=1}^{m} N_{p_j}) \cdot N \cdot n,$$

where n being the number of the fixed-point iterations for each enrichment step.

As comparison, the numerical complexity of the original high-dimensional problem Eq. (4) is

$$N_{\mathbf{x}} \cdot \prod_{j=1}^{m} N_{p_j}.$$

For example, assume a very coarse descriptions $N_{\mathbf{x}} = 1000$, $N_{p_j} = 10$, $m = 10$, $N = 50$ and $n = 20$, the numeric complexity is $1000 \times 10^{10} = 10^{13}$ for an FE approach while $(1000 + 10 \times 10) \times 50 \times 20 = 1.1 \times 10^{6}$ for the above approach.

7. Conclusion

This paper proposed a novel approach to achieve an instant simulation for cellular structures by applying it as computing solution to a high-dimension bi-scale FE analysis problem. This is achieved by computing offline a direct design-to-stress mapping, which is a general FE solution involving the design parameters in a high-dimension space where the design parameters are taken as extra coordinates in addition to the spatial coordinates. The recently developed model reduction technique, PGD, is extended to resolve the involved key issue of the curse of dimensionality, at both the micro- and macro-scales. As the experiment results demonstrate, the proposed approach works for various cellular structure design problems including editing or replacing the microstructures, changing their distributions, or changing the magnitude of the external loadings. It can also achieve a simulation with any level of accuracy almost without any loss of online simulation speed.

The proposed approach is still limited in several aspects. First, the instant online simulation is achieved at the cost of expensive offline computations. This issue can be overcome through a further separation of the variables, in either of the spatial coordinates. In addition, further use of parallel computation techniques can also help resolve this issue. Second, the approach mainly works for cellular structures consisting of microstructures homogeneously distributed or controlled by a few distribution parameters. Although such cases are popular and important in industrial design, further extending the approach to arbitrary types of microstructure designs is still a particularly challenging and interesting topic that deserves further research efforts.

Declaration of competing interest

The authors declare that they have no known competing financial interests or personal relationships that could have appeared to influence the work reported in this paper.

Acknowledgments

The work described in this paper is partially supported by the National Key Research and Development Program of China (No. 2018YFB1700603) and the NSF of China (No. 61872320).

Appendix A. Supplementary data

Supplementary material related to this article can be found online at https://doi.org/10.1016/j.visinf.2019.07.002.

References

Ammar, A., Mokdad, B., Chinesta, F., Keunings, R., 2006. A new family of solvers for some classes of multidimensional partial differential equations encountered in kinetic theory modeling of complex fluids. J. Non-Newton. Fluid Mech. 139 (3), 153–176.

Ammar, A., Mokdad, B., Chinesta, F., Keunings, R., 2007. A new family of solvers for some classes of multidimensional partial differential equations encountered in kinetic theory modelling of complex fluids: Part II: Transient simulation using space–time separated representations. J. Non-Newton. Fluid Mech. 144 (2), 98–121.

Andreassen, E., Andreasen, C.S., 2014. How to determine composite material properties using numerical homogenization. Comput. Mater. Sci. 83, 488–495.

Ashby, M.F., Medalist, R.F.M., 1983. The mechanical properties of cellular solids. Metall. Trans. A 14 (9), 1755–1769.

Bader, B.W., Kolda, T.G., et al., 0000. Matlab tensor toolbox version 3.0-dev, Available online (Oct. 2017). URL https://www.tensortoolbox.org.

Barbič, J., 2012. FEM Simulation of 3D deformable solids: A practitioner's guide to theory, discretization and model reduction. Part 2: Model reduction. In: ACM SIGGRAPH 2012 Courses. ACM, pp. 1–15.

Barbič, J., Zhao, Y., 2011. Real-time large-deformation substructuring. ACM Trans. Graph. 30 (4), 91:1–91:8.

Bendsøe, M.P., Kikuchi, N., 1988. Generating optimal topologies in structural design using a homogenization method. Comput. Methods Appl. Mech. Engrg. 71 (2), 197–224.

Białecki, R., Kassab, A., Fic, A., 2005. Proper orthogonal decomposition and modal analysis for acceleration of transient fem thermal analysis. Internat. J. Numer. Methods Engrg. 62 (6), 774–797.

Chen, Y., 2007. 3D texture mapping for rapid manufacturing. Comput.-Aided Des. Appl. 4 (6), 761–771.

Chen, J., Bao, H., Wang, T., Desbrun, M., Huang, J., 2018. Numerical coarsening using discontinuous shape functions. ACM Trans. Graph. 37 (4), 1–12.

Chen, Y., Wang, S., 2008. Computer-aided product design with performance-tailored mesostructures. Comput.-Aided Des. Appl. 5 (1–4), 565–576.

Chen, X., Zheng, C., Zhou, K., 2017. Example-based subspace stress analysis for interactive shape design. IEEE Trans. Vis. Comput. Graphics (10), 2314–2327.

Chinesta, F., Ammar, A., Cueto, E., 2010. Recent advances and new challenges in the use of the proper generalized decomposition for solving multidimensional models. Arch. Comput. Methods Eng. 17 (4), 327–350.

Chinesta, F., Ammar, A., Leygue, A., Keunings, R., 2011a. An overview of the proper generalized decomposition with applications in computational rheology. J. Non-Newton. Fluid Mech. 166 (11), 578–592.

Chinesta, F., Ladeveze, P., Cueto, E., 2011b. A short review on model order reduction based on proper generalized decomposition. Arch. Comput. Methods Eng. 18 (4), 395.

Cueto, E., González, D., Alfaro, I., 2016. Proper Generalized Decompositions: An Introduction To Computer Implementation with Matlab. Springer.

Falcó, A., Nouy, A., 2011. A proper generalized decomposition for the solution of elliptic problems in abstract form by using a functional eckart-young approach. J. Math. Anal. Appl. 376 (2), 469–480.

Fleck, N., Deshpande, V., Ashby, M., 2010. Micro-architectured materials: past, present and future. Proc. R. Soc. A 466 (2121), 2495–2516.

Fullwood, D.T., Niezgoda, S.R., Adams, B.L., Kalidindi, S.R., 2010. Microstructure sensitive design for performance optimization. Prog. Mater. Sci. 55 (6), 477–562.

Ganapathysubramanian, B., Zabaras, N., 2007. Modeling diffusion in random heterogeneous media: Data-driven models, stochastic collocation and the variational multiscale method. J. Comput. Phys. 226 (1), 326–353.

Gibson, L.J., Ashby, M.F., 1997. Cellular Solids: Structure and Properties. Cambridge university press.

Gielis, J., 2003. A generic geometric transformation that unifies a wide range of natural and abstract shapes. Am. J. Bot. 90 (3), 333–338.

Huang, X., Zhou, S., Sun, G., Li, G., Xie, Y.M., 2015. Topology optimization for microstructures of viscoelastic composite materials. Comput. Methods Appl. Mech. Engrg. 283, 503–516.

Kim, D., Koh, W., Narain, R., Fatahalian, K., Treuille, A., O'Brien, J.F., 2013. Near-exhaustive precomputation of secondary cloth effects. ACM Trans. Graph. 32 (4), 87:1–87:8.

Kolda, T.G., Bader, B.W., 2009. Tensor decompositions and applications. SIAM Rev. 51 (3), 455–500.

Lamari, H., Ammar, A., Cartraud, P., Legrain, G., Chinesta, F., Jacquemin, F., 2010. Routes for efficient computational homogenization of nonlinear materials using the proper generalized decompositions. Arch. Comput. Methods Eng. 17 (4), 373–391.

Li, S., Huang, J., de Goes, F., Jin, X., Bao, H., Desbrun, M., 2014. Space–time editing of elastic motion through material optimization and reduction. ACM Trans. Graph. 33 (4), 108:1–108:10.

Liu, X., Shapiro, V., 2017. Sample-based synthesis of two-scale structures with anisotropy. Comput. Aided Des. 90, 199–209.

Lu, L., Sharf, A., Zhao, H., Wei, Y., Fan, Q., Chen, X., Savoye, Y., Tu, C., Cohen-Or, D., Chen, B., 2014. Build-to-last: Strength to weight 3D printed objects. ACM Trans. Graph. 33 (4), 97:1–97:10.

Olson, G.B., 1997. Computational design of hierarchically structured materials. Science 277 (5330), 1237–1242.

Panchal, J.H., Kalidindi, S.R., McDowell, D.L., 2013. Key computational modeling issues in integrated computational materials engineering. Comput. Aided Des. 45 (1), 4–25, Computer-aided multi-scale materials and product design.

Panetta, J., Rahimian, A., Zorin, D., 2017. Worst-case stress relief for microstructures. ACM Trans. Graph. 36 (4), 122:1–122:16.

Panetta, J., Zhou, Q., Malomo, L., Pietroni, N., Cignoni, P., Zorin, D., 2015. Elastic textures for additive fabrication. ACM Trans. Graph. 34 (4), 135:1–135:12.

Regli, W., Rossignac, J., Shapiro, V., Srinivasan, V., 2016. The new frontiers in computational modeling of material structures. Comput. Aided Des. 77, 73–85.

Rodrigues, H., Guedes, J., Bendsoe, M., 2002. Hierarchical optimization of material and structure. Struct. Multidiscip. Optim. 24 (1), 1–10.

Rvachev, V.L., Sheiko, T.I., 1995. R-functions in boundary value problems in mechanics. Appl. Mech. Rev. 48 (4), 151–188.

Schulz, A., Xu, J., Zhu, B., Zheng, C., Grinspun, E., Matusik, W., 2017. Interactive design space exploration and optimization for CAD models. ACM Trans. Graph. 36 (4), 157:1–157:14.

Schumacher, C., Bickel, B., Rys, J., Marschner, S., Daraio, C., Gross, M., 2015. Microstructures to control elasticity in 3d printing. ACM Trans. Graph. 34 (4), 136:1–136:13.

Shapiro, V., 1991. Theory of R-functions and applications: A primer, Cornell University.

Sigmund, O., 1994. Materials with prescribed constitutive parameters: An inverse homogenization problem. Int. J. Solids Struct. 31 (17), 2313–2329.

Sigmund, O., Maute, K., 2013. Topology optimization approaches. Struct. Multidiscip. Optim. 48 (6), 1031–1055.

Treuille, A., Lewis, A., Popović, Z., 2006. Model reduction for real-time fluids. ACM Trans. Graph. 25 (3), 826–834.

Umetani, N., Kaufman, D.M., Igarashi, T., Grinspun, E., 2011. Sensitive couture for interactive garment modeling and editing. ACM Trans. Graph. 30 (4), 90:1–90:12.

Wang, L., Bertoldi, K., 2012. Mechanically tunable phononic band gaps in three-dimensional periodic elastomeric structures. Int. J. Solids Struct. 49 (19), 2881–2885, Proceedings of International Union of Theoretical and Applied Mechanics Symposium.

Wang, W., Wang, T.Y., Yang, Z., Liu, L., Tong, X., Tong, W., Deng, J., Chen, F., Liu, X., 2013. Cost-effective printing of 3D objects with skin-frame structures. ACM Trans. Graph. 32 (6), 177:1–177:10.

Wu, J., Aage, N., Westermann, R., Sigmund, O., 2018. Infill optimization for additive manufacturing-approaching bone-like porous structures. IEEE Trans. Vis. Comput. Graphics 24 (2), 1127–1140.

Wu, J., Dick, C., Westermann, R., 2016. A system for high-resolution topology optimization. IEEE Trans. Vis. Comput. Graphics 22 (3), 1195–1208.

Xu, C., Gao, S., Li, M., 2017a. A novel PCA-based microstructure descriptor for heterogeneous material design. Comput. Mater. Sci. 130, 39–49.

Xu, H., Li, Y., Chen, Y., Barbič, J., 2015. Interactive material design using model reduction. ACM Trans. Graph. 34 (2), 18:1–18:14.

Xu, C., Li, M., Huang, J., Gao, S., 2017b. Efficient biscale design of semiregular porous structures with desired deformation behavior. Comput. Struct. 182, 284–295.

Zhu, L., Li, M., Martin, R.R., 2016. Direct simulation for CAD models undergoing parametric modifications. Comput. Aided Des. 78, 3–13.

Zhu, B., Skouras, M., Chen, D., Matusik, W., 2017. Two-scale topology optimization with microstructures. ACM Trans. Graph. 36 (5), 164:1–164:16.